Ashraq M. Kadim
Khalid H. Abass

Department of Physics, College of Education for Pure Sciences, University of Babylon, Hilla, IRAQ

Synthesis of Silver Telluride Nanoparticles via Chemical Co-Precipitation Method for Antibacterial Applications

Silver tellurides (Ag_2Te) quantum dots (QDs) have gained much attention in biological applications due to their unique photoluminescence properties and good biocompatibility. In this study, the chemical co-precipitation method was used to successfully produce Ag_2Te. Several methods were used to examine the morphological, structural, and optical characteristics of the produced NPs, including XRD, FE-SEM, EDX, FT-IR spectroscopy, and UV-visible and their antimicrobial activity was studied against bacteria. FESEM analysis displayed the shape of NPs to be irregular shape, the mean particle size is within the range were 30-100 nm. The x-ray diffraction results showed that the NPs structure is monoclinic. The UV-visible spectrum showed the absorption in the range 330 nm with a band gap energy of 2.7 eV. Wemple Di-Domenico's Single Effective Oscillator Model was used to calculate refractive-index dispersion as well as other associated parameters. According to the findings, nanoparticles displayed antibacterial properties, implying that they could be employed in medicine.

Keywords: Silver telluride; Quantum dots; Nanoparticles; Chemical co-precipitation
Received: 24 January 2025; **Revised:** 10 March 2025; **Accepted:** 17 March 2025

1. Introduction

Metal nanoparticles are important because of their unique electrical, optical, and physiochemical properties that differ greatly from those of bulk materials [1]. Large surface area, quantum effect, and small size effect silver NPs show outstanding performance in a variety of domains, including medication delivery, gene therapy, optics, and optoelectronics. Metal tellurides' distinct physical characteristics have garnered a lot of interest. The four most prevalent stable phases of the Ag_2Te class of compounds, which have different stoichiometries, are Ag_5Te_3, Ag_2Te, AgTe, and Ag_7Te_4 [2]. Ag_2Te has drawn a lot of attention lately because of its intriguing and practical properties [3]. With its promising thermoelectric properties, high electrical conductivity, and huge magnetoresistance, Ag_2Te is a major semiconductor (A2IBIV group) with a wide range of applications in solar cells, biological systems, and nonlinear optical devices. Ag_2Te NPs enhanced electrical conductivity can be attributed to two factors: (i) higher Charge carrier mobility and (ii) higher carrier concentration [4–9].

Reduced heat conductivity is linked to increased phonon scattering at the Ag_2Te NPs interface. The antimicrobial effect is determined using agar diffusion screening [10-12]. Agar diffusion-based tests, such as disc diffusion, well diffusion, agar plug, and agar spot assays, are frequently used and inexpensive procedures for assessing the antimicrobial activity of test materials. These methods depend on the antimicrobial substances dispersing into the surrounding agar medium through paper discs, wells, or plugs. This stops the bacteria that was injected from growing on the agar surface [13,14]. The purpose of this work is to describe the synthesis and characterization of Ag_2Te NPs via co-precipitation technique. XRD FE-SEM, EDX and UV-visible spectroscopies were used to characterize the produced Ag_2Te NPs. In addition, Ag_2Te NP's antibacterial properties have been assessed.

2. Experimental Procedures

Ag_2Te NPs were prepared using the co-precipitation technique. Firstly, 0.62 g of TeO_2 was dispersions in 100 ml of Ethylene glycol ($C_2H_4(OH)_2$) under stirring for 30 min at 120 °C. After that, 0.44 g of potassium hydroxide (KOH) was gradually added to the solution mentioned above. A magnetic stirrer was used to separately dissolve 0.74 g of ascorbic acid ($C_6H_8O_6$) in 10 ml of deionized water. The ascorbic solution was added to the TeO_2 suspension. After this, To make 1.2 M of silver nitrate ($AgNO_3$) solution, 1 g of $AgNO_3$ was dissolved in 10 ml of deionized water. Then, the $AgNO_3$ solution was added to the mixture solution. Finally, a black precipitate was produced indicating the formation of Ag_2Te NPs.

The Ag_2Te NPs was centrifuged for separation at 3000 rpm for about 30 min. To get rid of impurities, the Ag_2Te NPs was cleaned six times using distilled water and ethanol. Then, the pure Ag_2Te NPs was dried in the oven at 80 °C for 3 h Finally the NPs were crushed using a mortar and pestle to make fine Ag_2Te NPs and stored in a clean bottle for further characterization and activity evaluation.

A MIRA III Tescan field-emission scanning electron microscope (FE-SEM) with energy-dispersive x-ray spectroscopy (EDX) analysis was used to characterize the sample. FE-SEM provides information

about the surface morphology of the sample, while EDX is used for elemental analysis of the prepared. The phase and crystalline structure were characterized using PW1730 Philips X-ray diffractometer (XRD). Using a universal ATR sampling accessory and a spectral range of 4000 to 500 cm^{-1}, the Fourier-transform infrared (FT-IR) spectroscopy was utilized to examine the functional groups involved in the formation of nanoparticles. After that, at room temperature, measurements in the 200–800 nm wavelength range were conducted, the materials were placed in quartz cuvette cells having a route length of 1 cm.

3. Results and Discussion

The crystallinity of as prepared Ag_2Te NPs was examined using x-ray diffraction (XRD), as illustrated in Fig. (1). XRD investigations revealed that Ag_2Te NPs have a monoclinic structure. This is consistent with the literature data for Ag_2Te (standard JCPDS card file, 01-081-1985). As documented in the literature [15,16]. Diffraction peaks verified that Ag_2Te was in its crystalline form at 2θ =26.2851° (200), 28.2196° (-112), 29.9724° (111), 31.0735° (-212), 33.2633° (210), 38.0412° (-312), 39.2267 ° (112), 40.0442° (-311), 41.2868° (313), 42.1831° (211), 44.7379 ° (-402), 47.133° (-314), 51.562° (-123), and 54.1551° (-321), and 64.459° (-421), and 67.3267° (-225), and 77.3892° (421).

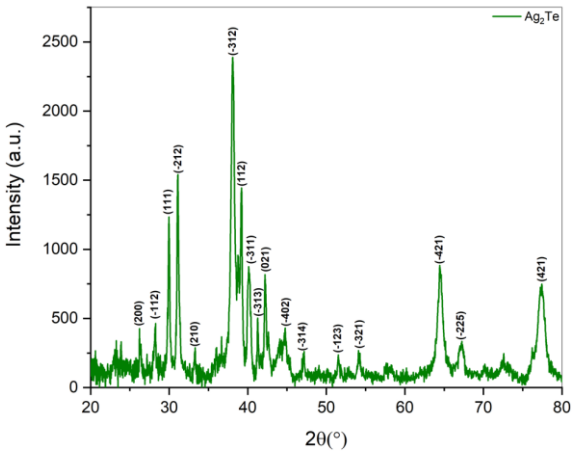

Fig. (1) XRD pattern of Ag_2Te NPs

The XRD pattern shows no undesired phases belonging to any structure, verifying the products' purity. The inherent strain effect and the crystallite size effect both cause the XRD peak in nanocrystals to broaden. Typically, this peak broadening is divided into two categories: instrumental broadening and physical broadening. The following relation yields the revised instrumental broadening [16]:

$$(\beta_D)^2 = (\beta_m)^2 - (\beta_i)^2 \quad (1)$$

where β_i represents the instrumental broadening, β_m represents the measured broadening, and β_D represents the corrected broadening. FWHM is used to quantify the sample's physical and instrumental widening .The Scherrer equation can be used to calculate the average crystallite size [24]. Using modified physical broadening, the crystallite size, calculated using the Scherrer equation, was found to be 30.5 nm.

$$D = \frac{k\lambda}{\beta cos\theta} = \frac{0.9\lambda}{\beta cos\theta} \quad (2)$$

$$\frac{1}{d_{hkl}^2} = \frac{h^2}{a^2} + \frac{k^2}{b^2} + \frac{l^2}{c^2} \quad (3)$$

where the Miller indices are denoted by hkl and the inter-planar spacing by d_{hkl}. Table (1) contains a list of every parameter that was established using the XRD data. Grain boundaries, point defects, stacking faults, and triple junctions can all cause intrinsic strain in nanocrystals, which is not taken into consideration by the Debye-Scherrer formula, which only considers the effect of crystalline size on the broadening of XRD peaks [18–20].

Table (1) Structural parameters of Ag_2Te NPs matched by JCPDS card no. 01-081-1985

2θ (deg)	hkl	FWHM (deg)	2θ (rad)	FWHM (rad)	D (nm)
26.2851	200	0.20467	0.229	0.004	22
28.2196	-112	0.1535	0.246	0.003	45.8
29.9724	111	0.1535	0.262	0.003	55.6
31.0735	-212	0.1535	0.271	0.003	70.6
33.2633	210	0.30701	0.290	0.005	19.6
38.0412	-312	0.1535	0.332	0.003	47.1
39.2267	112	0.17909	0.342	0.003	17.2
40.0442	-311	0.40934	0.349	0.007	47.4
41.2868	313	0.1535	0.360	0.003	57.5
42.1831	021	0.1535	0.368	0.003	23.4
44.7379	-402	0.30701	0.390	0.005	28.5
47.133	-314	0.09	0.411	0.002	11.9
51.562	-123	0.61402	0.450	0.011	18.2
54.1551	-321	0.30701	0.473	0.005	15.2
64.459	-421	0.25584	0.563	0.004	15.5
67.3267	-225	0.61402	0.588	0.011	11.7
77.3892	421	0.81869	0.675	0.014	12.42
Mean Crystallite Size					**30.5**

Figure (2a,b) represents the FE-SEM images Surface morphology and the shape of the synthesized Ag_2Te NPs were deduced at different magnifications by FE-SEM as illustrated in Fig. (2c), the particle had an irregular shape with varying sizes. The particle size distribution was irregular, with most particles ranging in diameter from 30 to 100 nm. In addition, the size distribution of the prepared Ag_2Te NPs was shown as a histogram in Fig. (2c). The average diameter of these NPs is 59.6 nm. The average diameter of the Ag_2Te NPs was determined using the Image J analysis. The elemental makeup of the produced Ag_2Te NPs was verified using the EDX. The EDX spectrum Fig. (2c) suggests the existence of silver (Ag) and telluride (Te) elements. Showed an optical absorption band peak of silver Ag at approximately 2.5 keV, the weight of Ag and Te is 81.4% and 18.6%, respectively [21-23].

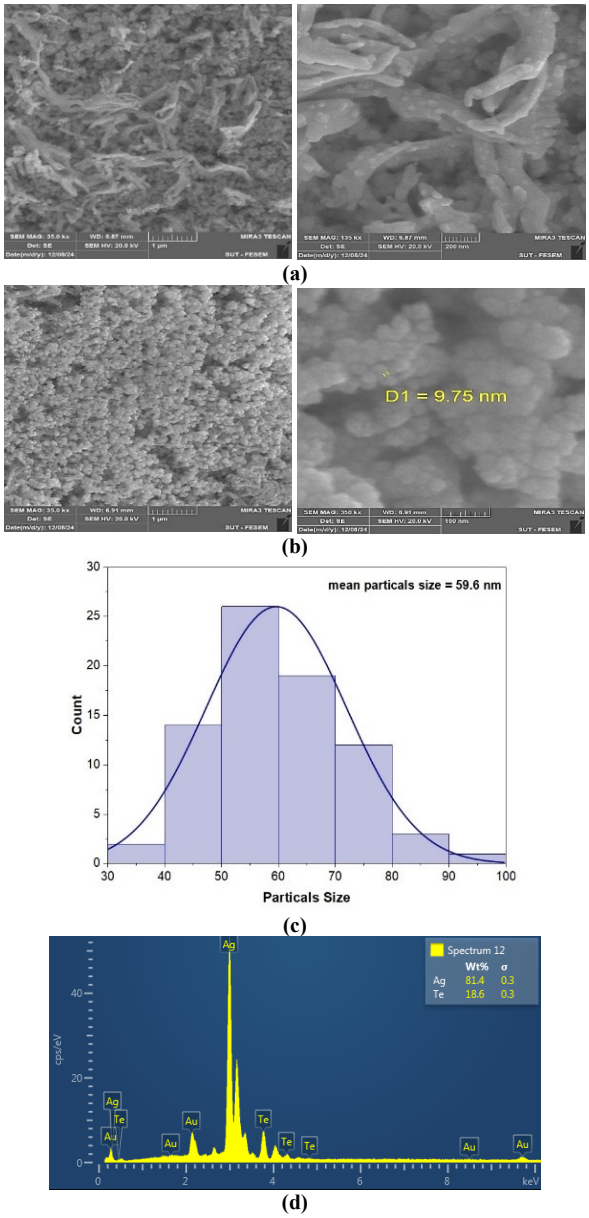

Fig. (2) FE-SEM images (a and b at different magnification), (c) Histogram of Particle Size NPs, (d) (EDX) spectrum of Ag_2Te

The chemical composition of Ag_2Te nanoparticles was investigated using the FT-IR method. According to Fig. (3a) very strong and broad band at about 3446.79 cm^{-1} is observed which is attributed to O-H vibrations absorbed from moisture. The peak at 2987.74 cm^{-1} is attributed to C-H stretching. These asymmetric C-H and N-H stretching vibrations are related to the band seen at 2893.22 cm^{-1} which may be due to the residual organic matter in the sample. While the bands at 1716.65 cm^{-1} were assigned to C=O stretching that may be related to the vibrations of carbonyl residues, the stretching of the C–C functional group was confirmed by the peak values occurring at 1425.40 cm^{-1}, and the peaks observed at 993.34–430.13 cm^{-1} are related to the lattice vibrations and Ag–Te bonds [24–25].

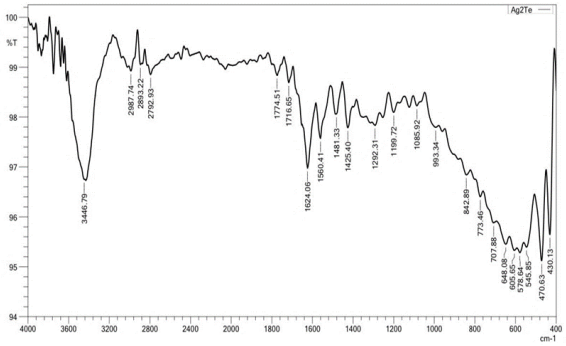

Fig. (3) FTIR spectra of pure Ag_2Te NPs

The UV-visible absorption is displayed in Fig. (4a) an absorption peak at 330 nm confirms the successful formation of Ag_2Te NPs [26]. Therefore, the point where the tangent of the Tuac Plot intersects the energy axis (Fig. 4b) was determined to represent the energy band gap (E_g) of Ag_2Te NPs. This is supported by the following equation [27]:

$$\alpha h\nu = A\,(h\nu - E_g)^2 \qquad (4)$$

where E_g is the energy band gap, $h\nu$ is the photon energy, α is the absorption coefficient per unit thickness (i.e., $\alpha = 2.303A/t$), and A is a proportionality constant

The direct band gap of the samples was calculated by plotting $(\alpha h\nu)^2$. The Ag_2Te NPs were found to have an energy band gap of roughly 2.7 eV. This result is in good agreement with the energy band gap values of Ag_2Te that have been reported in the literature [28-30].

The dispersion is a crucial component that must be taken into consideration when choosing materials for prospective uses or optoelectronic device designs that utilize spectral dispersion. The Single Effective Oscillator Model (SEOM-WDD), put forth by Wemple-Di-Domenico, is the best model for analyzing these features of the dispersion energy parameters. Wemple and DiDomenico defined E_d and E_o by using a single oscillator model of the frequency-dependent dielectric constant [31].

$$(n^2 - 1) = \frac{E_d E_o}{[E_o^2 - (h\nu)^2]} \qquad (5)$$

Rearranging this equation to get:

$$(n^2 - 1)^{-1} = \frac{E_o^2 - (h\nu)^2}{E_d E_o} = \frac{E_o}{E_d} - \frac{(h\lambda)^2}{E_d E_o} \qquad (6)$$

Thus, the index of $(n^2\text{-}1)^{-1}$ versus $(h\nu)^2$ can be plotted and straight lines can be fitted to the points to represent this equation, as illustrated in Fig. (5). As a result, anyone can obtain a straight line with a slope equal to $[1/E_dE_o]$ and an intercept on the y-axis at a value supplied by this term (E_o/E_d). As such, For the NPs samples displayed in Fig. (5), the energy values of the dispersion (strength), Ed, and the effective single oscillator, E_o, can be computed. The values of E_o and E_d are given in table (2). The following relation can be used to derive the static refractive index (n_o) by evaluating $(n^2\text{-}1)^{-1}$ versus $(h\nu)^2$ [32]:

$$n_o = (1 + \frac{E_d}{E_o})^{\frac{1}{2}} \qquad (7)$$

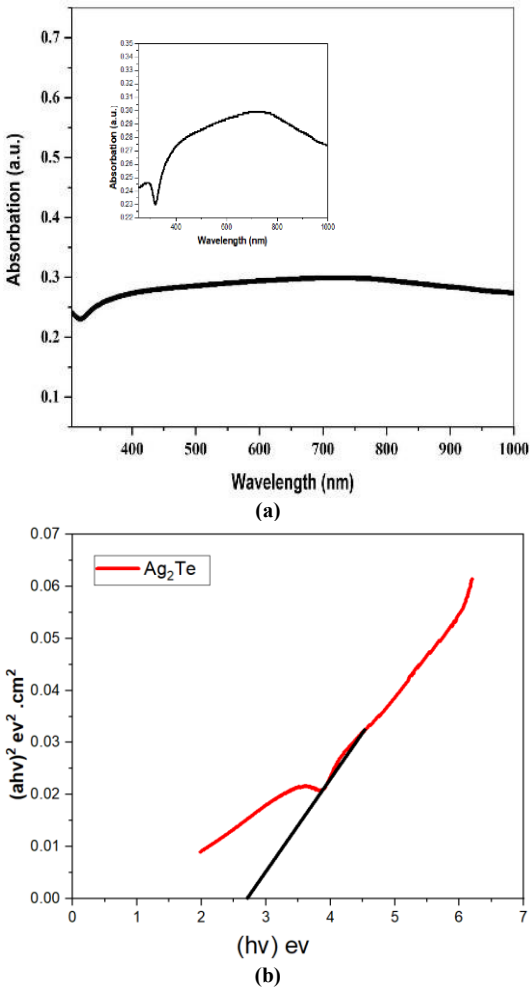

Fig. (4) (a) UV absorbance spectrum and b) energy band gab of a Ag_2Te NPs

Table (2) Some important optical characteristics that were estimated for the Ag_2Te NPs

E_oE_d	275
E_o^2	85.1125
E_o	9.225643609
E_g	4.612821804
E_d	29.80821845
$n^2(0)$	4.231017771
$n_o(0)$	2.056943794
ε	4.231017771
M_{-1}	3.231017771
M_{-3}	0.03796173

The incident photon energy (*hv*) approaches zero according to the Wemple-DiDomenico relationship. Table .2 shows the computed static refractive index (n_o) for all films. The [E_0] and [E_d] values from the fitted transmittance spectra are used to calculate the (M_{-1}) and (M_{-3}) moments of the optical spectra using two equations [33,34].

$$E_o^2 = \frac{M_{-1}}{M_{-3}} \quad (8)$$

$$E_d^2 = \frac{M_{-1}^3}{M_{-3}} \quad (9)$$

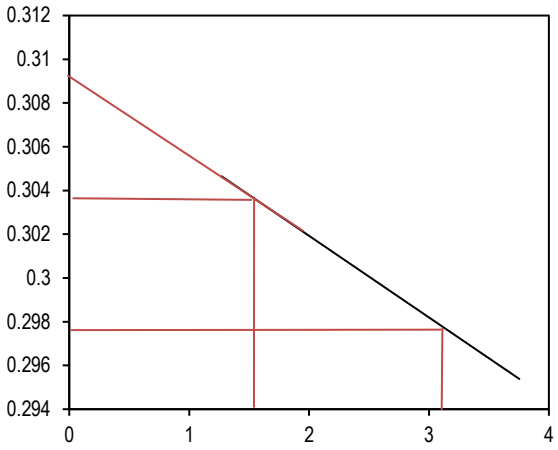

Fig. (5) Plot of $(n^2-1)^{-1}$with $(hv)^2$ for Ag_2Te NPs

The antibacterial performance of the Ag_2Te NPs was assessed using the agar well diffusion method, tested against two clinical pathogens used to investigate the bactericidal properties of these nanoparticles; *S. aureus* and *K. pneumoniae* as sources of both Gram-positive and Gram-negative bacteria, respectively. Mueller-Hinton agar plates were prepared for this purpose. A sterile tip was used to bore wells with a diameter of 6 mm on the agar plates after the organisms had been cultivated. Various concentrations of Ag_2Te NPs samples were used in the bored wells, four wells were made in each plate and were inoculated in each well. The cultured plates containing the samples (Ag_2Te) and test organisms were incubated at 37°C overnight. The zone of inhibition in response to the challenge was measured after 24 hours. Figures (6) and (7) illustrate zones of inhibition of *K. pneumoniae* and *S. aureus* against Ag_2Te NPs at concentrations ranging from 12.5 µg/mL to 100 µg/mL.

The nanoparticles showed a strong antibacterial effect of NPs. Table (3) displays the average zone of inhibition values (mm). The zone of inhibition for S. aureus was 15–17 mm, whereas *K. pneumoniae* was 17–19 mm. The inhibition zone increased as the concentration of nanoparticles was increased. Since Ag NPs have a very large surface area, they can make better contact with microorganisms and exhibit effective antibacterial properties. Depending on their size, the nanoparticles either adhere to the bacteria's surface or pass through their cell membrane [35].

Table (3) The antimicrobial properties of Ag_2Te NPs

Antibacterial analysis (inhibition zone (mm))					
Sample	A	B	C	D	E
K. pneumoniae	6	17	17.5	18	19
S. aureus	6	15	15.5	16.5	17

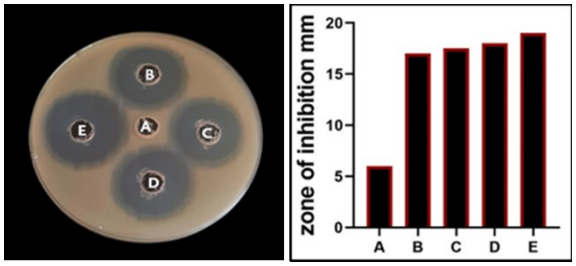

Fig. (6) Antimicrobial studies to various concentrations of Ag_2Te NPs against *K. pneumoniae* (A) control, (B) 12.5µg/mL, (C) 25µg/mL, (D) 50µg/mL, and (E) 100µg/mL

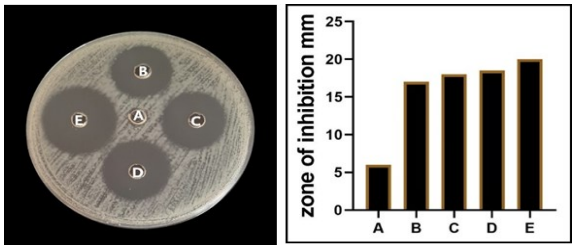

Fig. (7) Antimicrobial studies to various concentrations of Ag_2Te NPs against *S. aureus* (A) control, (B) 12.5µg/mL, (C) 25µg/mL, (D) 50µg/mL, and (E) 100µg/mL

5. Conclusion

In this paper, Ag_2Te nanoparticles were prepared by co-precipitation method. XRD studies indicated that the synthesized Ag_2Te NPs show a crystalline shape with a mean crystallite size of 30.5 nm. FE-SEM images revealed that the Ag_2Te NPs were irregular in shape with diameters of 30–100 nm. The synthesized Ag_2Te NPs showed an absorption peak at ~330nm. EDX results confirmed the presence of Te and Ag with a pure phase. Therefore, the synthesized Ag_2Te NPs proved to have antibacterial activity. Our results confirm the potential of Ag_2Te NPs synthesis in a simple, fast, and cost-effective.

References

[1] D.S Al-Namil et al., "Solid-state green synthesis of Ag NPs: Higher temperature harvests larger Ag NPs but smaller size has better catalytic reduction reaction", *Sci. Rep.,* 9(1) (2019) 15212.

[2] G.M. Li et al., "Morphological evolution, growth mechanism, and magneto-transport properties of silver telluride one-dimensional nanostructures", *Nanoscale Res. Lett.,* 8 (2013) 1-8.

[3] P. Velusamy et al., "Bio-inspired green nanoparticles: synthesis, mechanism, and antibacterial application", *Toxicol. Res.,* 32(2) (2016) 95-102.

[4] R.M. Kakhki, S. Hedayat and K. Mohammadzadeh, "Novel, green and low cost synthesis of Ag nanoparticles with superior adsorption and solar based photocatalytic activity", *J. Mater. Sci.: Mater. in Electron.,* 30(9) (2019) 8788-8795.

[5] A.K. Samal and T. Pradeep, "Room-temperature chemical synthesis of silver telluride nanowires", *The J. Phys. Chem. C*, 113(31) (2009) 13539-13544.

[6] Y. Chang et al., "Facile synthesis of Ag_2Te nanowires and thermoelectric properties of Ag_2Te polycrystals sintered by spark plasma sintering", *Cryst. Eng. Comm.*, 21(11) (2019) 1718-1727.

[7] X. Feng et al., "Simple synthesis of ultra-long Ag_2Te nanowires through solvothermal co-reduction method", *J. Solid State Chem.,* 183(10) (2010) 2382-2388.

[8] D.A. Hitchcock, "Unusually low thermal conductivity in the argyrodite Ag_8GeTe_6 attributed to strong anharmonicity", Dissert., Clemson University (2014).

[9] A.K. Gautam and N. Khare, "Enhanced thermoelectric figure of merit at near room temperature in n-type binary silver telluride nanoparticles", *J. Materiomics,* 9(2) (2023) 310-317.

[10] J. Ouyang et al., "Ag_2Te colloidal quantum dots for near-infrared-II photodetectors", *ACS Appl. Nano Mater.,* 4(12) (2021) 13587-13601.

[11] Y.-W. Liu et al., "Near-infrared absorption of monodisperse silver telluride (Ag_2Te) nanocrystals and photoconductive response of their self-assembled superlattices", *Chem. Mater.,* 23(21) (2011) 4657-4659.

[12] H. Yang et al., "Au-Doped Ag_2Te Quantum Dots with Bright NIR-IIb Fluorescence for *in situ* Monitoring of Angiogenesis and Arteriogenesis in a Hindlimb Ischemic Model", *Adv. Mater.,* 33(37) (2021) 2103953.

[13] B. Zhong et al., "Simple synthesis of crooked Ag_2Te nanotubes and their photoelectrical properties", *New J. Chem.,* 45(13) (2021) 6100-6107.

[14] Y. Wang et al., "Silver telluride colloidal quantum dot infrared photodetectors and image sensors", *Nature Photon.,* 18(3) (2024) 236-242.

[15] N. Kumar, S.S. Ray and J.C. Ngila, "Ionic liquid-assisted synthesis of Ag/Ag_2Te nanocrystals via a hydrothermal route for enhanced photocatalytic performance", *New J. Chem.,* 41(23) (2017) 14618-14626.

[16] H. Fukuyama et al., "New synthetic method of forming aluminum oxynitride by plasma arc melting", *J. Am. Cer. Soc.,* 82(6) (1999) 1381-1387.

[17] G.K. Williamson and R.E. Smallman, "III. Dislocation densities in some annealed and cold-worked metals from measurements on the X-ray debye-scherrer spectrum", *Philo. Mag.,* 1(1) (1956) 34-46.

[18] L. Li et al., "Ag as cocatalyst and electron-hole medium in CeO_2 QDs/Ag/Ag_2Se Z-scheme heterojunction enhanced the photo-

electrocatalytic properties of the photoelectrode", *Nanomater.,* 10(2) (2020) 253.
[19] S. Mishra et al., "A Facile Molecular Precursor-based Synthesis of Ag_2Se Nanoparticles and Its Composites with TiO_2 for Enhanced Photocatalytic Activity", *Chem. An Asian J.*, 11(11) (2016) 1658-1663.
[20] K. Nakaya and T. Nakaoka, "Single-crystalline Ag_2Te nanorods prepared by room temperature sputtering of GeTe", *SN Appl. Sci.,* 2(9) (2020) 1601.
[21] G.M. Li et al., "Morphological evolution, growth mechanism, and magneto-transport properties of silver telluride one-dimensional nanostructures", *Nanoscale Res. Lett.,* 8 (2013) 1-8.
[22] K. Hirata et al., "Magneto-thermal conductivity effect and enhanced thermoelectric figure of merit in Ag_2Te", *AIP Adv.,* 13(1) (2023).
[23] E. Kohan Baghkheirati et al., "Synthesis and antibacterial activity of stable bio-conjugated nanoparticles mediated by walnut (Juglans regia) green husk extract", *J. Exp. Nanosci.,* 11(7) (2016) 512-517.
[24] Z. Hu et al., "Enhanced thermoelectric performance in pristine $AgSbTe_2$ compound via rational design of Ag_2Te formation", *Acta Materialia*, 290 (2025) 120985.
[25] K. Abdali et al., "Morphological, Optical, Electrical Characterizations and Anti-*Escherichia coli* Bacterial Efficiency (AECBE) of PVA/PAAm/PEO Polymer Blend Doped with Silver NPs", *Nano Biomed. Eng.,* 14(2) (2022) 114-122.
[26] A.P. Yepseu et al., "Optical and photocatalytic properties of Cu_xS/ZnO composite thin films deposited by robotic spray pyrolysis deposition", *J. Nanomater.,* 2021(1) (2021) 9975600.
[27] J. Tauc, **"Amorphous and Liquid Semiconductors"**, Plenum Press (NY, 1974).
[28] A.M. Kadim et al., "Effect of loading corn starch nanoparticles on the morphological, optical, and dielectric behaviors of PVA/PMMA/PAAM polymer blend for optoelectronic and antibacterial applications", *Nano Biomed. Eng.,* 16(1) (2024) 119-127.
[29] O. Sentse et al., "A facile one-pot synthesis of Ag_2Te nanoparticles and the fabrication of nanocomposites for the removal of chromium (VI) in wastewater", *Inorg. Chem. Commun.*, 159 (2024) 111755.
[30] K.H. Abass and N.H. Obaid, "0.006 wt.% Ag-Doped Sb_2O_3 Nanofilms with various thickness: morphological and optical properties", *J. Phys.: Conf. Ser.*, 1294(2) (2019) 022005
[31] K.H. Abass and D.M. Latif, "The Urbach energy and dispersion parameters dependence of substrate temperature of CdO thin films prepared by chemical spray pyrolysis", *Int. J. Chem. Tech. Res.,* 9(9) (2016) 332-338.
[32] A.S. Hassanien, R. Neffati and K.A. Aly, "Impact of Cd-addition upon optical properties and dispersion parameters of thermally evaporated $Cd_xZn_{1-x}Se$ films: discussions on bandgap engineering, conduction and valence band positions", *Optik,* 212 (2020) 164681.
[33] H. Şafak, M. Merdan and Ö.F. Yüksel, "Dispersion analysis of SnS and SnSe", *Turk. J. Phys.,* 26(5) (2002) 341-348.
[32] P. Arun et al., "Optical linear-nonlinear and dispersion parameters of thermally evaporated SnS thin films as absorber material for solar cells", *Cond. Matter, arXiv:2301.07983* (2023).
[34] F.J. Hamood et al., "Preparation and Characterizations of PVA/Vanadium Nanocomposites for Gamma Ray Shielding and Antibacterial Activity Applications", *Int. J. Nanosci.,* 22(6) (2023) 2350049.
[35] F.J. Hamood et al., "Effect of CdS nanoparticles on structural, optical and dielectric properties for gamma-ray shielding and antibacterial efficiency of PVA/PAAm polymers blend", *Int. J. Nanosci.,* 22(5) (2023) 2350043.

